HOKKAIDO UNIVERSITY

Title	Coherent dynamics of exciton orbital angular momentum transferred by optical vortex pulses
Author(s)	Shigematsu, K.; Yamane, K.; Morita, R.; Toda, Y.
Citation	Physical Review B, 93(4), 045205-1-045205-8 https://doi.org/10.1103/PhysRevB.93.045205
Issue Date	2016-01-15
Doc URL	http://hdl.handle.net/2115/60593
Rights	©2016 American Physical Society
Type	article
File Information	PhysRevB.93.pdf

Instructions for use

Hokkaido University Collection of Scholarly and Academic Papers : HUSCAP

PHYSICAL REVIEW B **93**, 045205 (2016)

Coherent dynamics of exciton orbital angular momentum transferred by optical vortex pulses

K. Shigematsu, K. Yamane, R. Morita, and Y. Toda
Department of Applied Physics, Hokkaido University, Kita-13, Nishi-8, Kita-ku, Sapporo 060-8628, Japan

(Received 29 June 2015; revised manuscript received 2 October 2015; published 15 January 2016)

The coherent dynamics of the exciton center-of-mass motion in bulk GaN are studied using degenerate four-wave-mixing (FWM) spectroscopy with Laguerre-Gaussian (LG) mode pulses. We evaluate the exciton orbital angular momentum (OAM) dynamics from the degree of OAM, which is derived from the distributions of OAM (topological charge) of the FWM signals. When excitons are excited with two single-mode LG pulses, the exciton OAM decay time significantly exceeds the exciton dephasing time, which can be attributed to high uniformity of the exciton dephasing in our bulk sample because the decoherence of the exciton OAM is governed by the angular variation in the exciton dephasing. We also analyze the topological charge (ℓ) dependence of the OAM decay using a multiple-mode LG pump pulse, which allows us to simultaneously observe the dynamics of the exciton OAM for different ℓ values under the same excitation conditions. The OAM decay times of the $\ell = 1$ component are usually longer than those of the $\ell = 0$ component. The ℓ-dependent OAM decay is supported by a phenomenological model which takes into account the local nonuniformity of the exciton dephasing.

DOI: 10.1103/PhysRevB.93.045205

I. INTRODUCTION

Optical vortices have azimuthal phase structures that can be expressed as $\exp(i\ell\phi)$, where ℓ is an integer and ϕ is the azimuthal angle in the beam cross section, and these vortices carry orbital angular momentum (OAM) owing to the rotational energy flow vectors around phase singularities where the intensity of the fields vanishes. Since Allen *et al.* [1] demonstrated that a Laguerre-Gaussian (LG) beam with the azimuthal phase structure $\exp(i\ell\phi)$ carries an OAM of $\ell\hbar$ per photon, research on optical vortices has spread to various fields, including solid-state-device applications such as spintronics [2], information storage [3–5], processing [6–8], and quantum computation [9]. In such devices, information multiplexing using the OAM degree of freedom may significantly increase information capacity. Moreover, the topological aspects of OAM offer unique photoexcitations in semiconductors such as chiral imbalance of electrons [10], circular current [11,12], magnetic field [13,14], spin-polarized photoemission [15], and the photovoltaic effect [16]. In general, topological vortices are stable against continuous deformations, which is crucial for the above applications.

In our earlier studies, we demonstrated coherent excitations of the center-of-mass motion of semiconductor excitons with OAM via four-wave mixing (FWM) using LG pulses [17]. The dark centers associated with the phase singularities were observed in FWM signals, and their time evolution showed that the exciton OAM was coherently excited during the exciton dephasing time T_2. A similar result was reported by another group using a CdTe/CdZnTe quantum well sample [18]. Those characteristics were subsequently analyzed using OAM-resolved FWM spectroscopy [19], wherein the OAM spectra of the FWM signals indicated high purity of the exciton OAM when illuminated with single-mode LG pulses. However, while the time evolution of the FWM signals suggests that the decay of the exciton OAM should be longer than T_2, the details of the intrinsic decay dynamics, including robustness against scattering, disorder, and/or correlation, are still unclear.

In principle, the coherent FWM dynamics of excitons reflects the dephasing of exciton polarization induced by short-range disorder, wherein the spatial variations are averaged out over the optical excitation area. On the other hand, the OAM dephasing of the exciton center-of-mass motion results in transverse mode distributions and thus can provide information on the spatial variations in the dephasing.

In this study, we investigate the effects of spatially variant dephasing on the exciton OAM theoretically (Sec. II) and experimentally (Secs. III and IV). In the experiments, the exciton OAM dynamics is evaluated by the degree of OAM in the OAM spectra of the FWM signal. The exciton OAM with the topological charge of $\ell = +4$ shows a subnanosecond decay, which is considerably longer than T_2 (Sec. IV A). We also demonstrate the topological charge dependence of the exciton OAM dynamics, wherein a multiple-mode LG pulse is used as one of the excitation pulses to compare the OAM decay for different values of ℓ. The decay of the $\ell = +1$ component is usually longer than that of the $\ell = 0$ component (Sec. IV B). The ℓ-dependent OAM decay is discussed in terms of the spatially dependent dephasing (Sec. V).

II. COHERENT DYNAMICS OF EXCITON OAM

We analyze the exciton OAM via degenerate FWM using LG pulses. We first examine the FWM process in Fig. 1, where we consider a two-level exciton system for simplicity. As shown in Fig. 1(a), we use a pair of pulses with a degenerate frequency of ω_0, wave vectors $\mathbf{k}_i$, and topological charge ℓ_i, where $i = 1$ and 2 represent the pump and probe pulses, respectively. The pump pulse with wave vector $\mathbf{k}_1$ first excites the system to a coherent superposition state between the ground and excited states, thereby creating exciton polarization [see Fig. 1(b)]. The polarization immediately undergoes dephasing after the excitation. When the probe pulse with wave vector $\mathbf{k}_2$ arrives within the polarization dephasing time, the pulse promotes the system to the excited state or back to the ground state according to the phase of polarization. In real space, this process produces a spatially modulated excited-state grating, and its decay is governed by the dephasing of the exciton polarization. The probe pulse is then self-diffracted into the direction $2\mathbf{k}_2 - \mathbf{k}_1$ by the grating.

©2016 American Physical Society

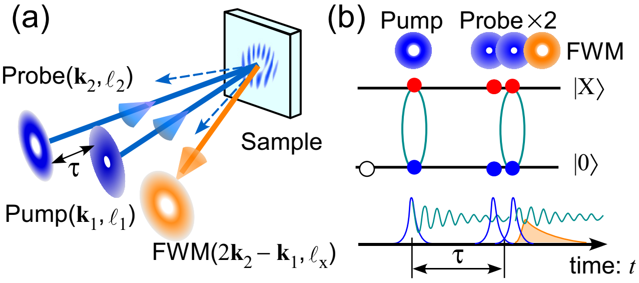
(a)
Probe($\mathbf{k}_2,\ell_2$)
τ
Pump($\mathbf{k}_1,\ell_1$)
Sample
FWM($2\mathbf{k}_2-\mathbf{k}_1,\ell_x$)
(b)
Pump
Probe×2
FWM
|X⟩
|0⟩
τ
time: t

FIG. 1. Schematic of four-wave mixing (FWM) using Laguerre-Gaussian pulses in (a) real space and (b) the corresponding time sequence. For simplicity, a two-level exciton system is presented in (b).

The exciton dephasing dynamics are thus obtained by detecting the signal as a function of the delay time τ between the pump and probe pulses [20–24].

For single-mode LG pulses with $\ell_i \neq 0$, the excited-state grating generates forklike fringes, and the resulting self-diffracted FWM signal exhibits an LG mode with $\ell = 2\ell_2 - \ell_1$ if the excitons completely conserve the OAM in the FWM process. On the other hand, the spatial distributions of scattering, disorder, and/or correlation induce angular modulations on the exciton coherence and generate the $\ell \neq 2\ell_2 - \ell_1$ components in the FWM signal based on the Fourier relationship between the angular position and OAM [25,26]. Therefore, we can evaluate the coherent dynamics of the exciton OAM by measuring the distribution of ℓ, i.e., the OAM spectrum [27,28] of the FWM signal. In the experiments, the OAM spectra were obtained with the mode conversion technique using a spatial light modulator (SLM) [9,29]. Programmable holograms on the SLM decompose the FWM signal into a series of LG components with different values of ℓ.

Here, we introduce descriptions of the FWM using LG pulses for the exciton OAM dynamics. In the case when $\mathbf{k}_i/|\mathbf{k}_i| \approx \mathbf{e}_z$, where $\mathbf{e}_z$ denotes the unit vector along the z direction, the incident electric field for colinearly polarized pump and probe pulses can be written in the cylindrical coordinates (r,ϕ,z) as

$$\begin{aligned} E(r,\phi,z,t,\tau) &= E_1(r,\phi,z)A(t) + E_2(r,\phi,z)A(t-\tau) \\ &\propto U_{\ell_1}(r)A(t)\exp[i(k_1 z + \ell_1\phi - \omega_0 t)] \\ &\quad + U_{\ell_2}(r)A(t-\tau)\exp[i(k_2 z + \ell_2\phi - \omega_0 t)]. \end{aligned} \tag{1}$$

Here, $A(t)$ represents the temporal envelope of the optical pulses. We define the delay time $\tau > 0$ when the pump pulse precedes the probe pulse. The amplitude distribution of an LG mode $U_\ell(r)$ is

$$U_\ell(r) = \sqrt{\frac{2}{\pi|\ell|!}}\frac{1}{w}\left(\frac{\sqrt{2}r}{w}\right)^{|\ell|}\exp(-r^2/w^2), \tag{2}$$

where w is a parameter associated with the beam size. The distribution $U_\ell(r)$ corresponds to a ring-shaped intensity profile for an LG beam with ring radius ρ (the distance between the beam center and the position at which the LG beam exhibits its peak intensity) defined by

$$\rho = \sqrt{\frac{|\ell|}{2}}w. \tag{3}$$

It is to be noted that $U_0(r)$ corresponds to a Gaussian distribution and the ring radius ρ is thus undefined.

When the pulse duration is considerably shorter than the exciton dephasing time, $A(t)$ can be treated as a δ function. The third-order nonlinear polarization $P^{(3)}$ (along the $2\mathbf{k}_2 - \mathbf{k}_1$ direction) induced by the LG pump and probe pulses is subsequently expressed as

$$\begin{aligned} P^{(3)}(r,\phi,z,t,\tau) &\propto \Theta(t-\tau)\alpha(r,\phi,t)U_{\ell_1}(r)U_{\ell_2}^2(r) \\ &\quad\times \exp[i\{(2k_2-k_1)z + (2\ell_2-\ell_1)\phi\}], \end{aligned} \tag{4}$$

where $\Theta(t-\tau)$ represents the Heaviside step function. The term $\alpha(r,\phi,t,\tau)$ associated with the exciton system is expressed as

$$\begin{aligned} \alpha(r,\phi,t,\tau) &= |\mu_x(r,\phi)|^4\exp[-i\omega_x(t-2\tau)] \\ &\quad\times \exp[-\gamma(r,\phi)t], \end{aligned} \tag{5}$$

where both the dipole matrix element μ_x and dephasing rate γ exhibit spatial variation owing to the spatially dependent scattering, disorder, and/or correlation. It is to be noted that we neglect the spatial variation in the resonance energy ω_x.

In the time evolution of the exciton polarization, $\gamma(r,\phi)$, i.e., spatially dependent dephasing, modulates the angular distribution of the exciton center-of-mass motion and generates a distribution of ℓ in the OAM spectrum. In order to verify the effects of spatially dependent dephasing $\gamma(r,\phi)$, we consider the Fourier relationship between the OAM and angular distribution for the exciton polarization $P^{(3)}(r,\phi,z,t,\tau)$ in Eq. (4). The relationship is described as follows [25,26]:

$$P^{(3)}(r,\phi,z,t,\tau) = \frac{1}{\sqrt{2\pi}}\sum_{\ell=-\infty}^{\infty} C(\ell,r,t,\tau)\exp[i\ell\phi], \tag{6}$$

$$\begin{aligned} C(\ell,r,t,\tau) &= \frac{1}{\sqrt{2\pi}}\int_{-\pi}^{\pi} P^{(3)}(r,\phi,z,t,\tau)\exp[-i\ell\phi]d\phi \\ &\propto \Theta(t-\tau)U_{\ell_1}(r)U_{\ell_2}^2(r)\int_{-\pi}^{\pi}\exp[-\gamma(r,\phi)t] \\ &\quad\times \exp[-i(\ell-\ell_x)\phi]d\phi, \end{aligned} \tag{7}$$

where $\ell_x = 2\ell_2 - \ell_1$, and we neglect the spatial dependence of μ_x to restrict ourselves to consider the effects of the spatially dependent dephasing $\gamma(r,\phi)$. The OAM spectrum of the FWM signal is obtained from $C(\ell,r,t,\tau)$ in Eq. (7) as

$$I_{\mathrm{FWM}}(\ell,\tau) \propto \int_\tau^\infty dt\int_0^\infty r|C(\ell,r,t,\tau)|^2 dr. \tag{8}$$

It is apparent from Eqs. (7) and (8) that if the exciton dephasing rate γ is spatially (azimuthally) uniform, $C(\ell,r,t,\tau)$ can be described by δ_{ℓ,ℓ_x}. As a result, there is a single nonzero component at $\ell = \ell_x$ in the OAM spectrum. On the other hand, the spatially (azimuthally) dependent dephasing $\gamma(r,\phi)$ yields nonzero $C(\ell,r,t,\tau)$ for $\ell \neq \ell_x$ and therefore induces spectral broadening in the OAM spectrum. This indicates that the spatially dependent dephasing $\gamma(r,\phi)$ results in decoherence of the exciton OAM, and the time-resolved measurement (i.e., measuring the τ dependence) of the OAM spectrum of the FWM signal allows us to evaluate the exciton OAM decoherence.

III. EXPERIMENT

In the experiments, the pulses of ~175 fs from a frequency-doubled mode-locked Ti: sapphire laser (repetition rate of 76 MHz) were used to perform the two-pulse degenerate FWM measurements. The center wavelength ($\lambda_0 = 2\pi c/\omega_0$) of 356.4 nm with the spectral width of 1.1 nm was selected to resonantly excite the exciton resonances of GaN. In our measurements, the exact λ_0 was slightly changed (±0.5 nm) to optimize the resonance condition. The colinearly polarized two pulses were converted into LG modes and focused onto the sample with a lens ($f = 200$ mm). The FWM signal in the reflection geometry was detected either with a charge-coupled device (CCD) camera or with a monochromator equipped with a CCD after passing through another mode conversion setup for the OAM-resolved measurements. The average power before the focusing lens was fixed to be ~1 mW for both the pump and probe beams. The beam radius on the sample was estimated to be ~50 μm. The total group-delay dispersion induced by our experimental setup was evaluated to be 2300 fs^2, which resulted in the pulse duration of ~190 fs on the sample. For the LG mode conversions for the excitation and signal detection, we used programmable holographic gratings on SLMs (Hamamatsu Photonics, X10468), where the pixel size is 20 μm with a pitch of 0.2 μm. The sample of a free-standing GaN (thickness of 70 μm) grown using a lateral epitaxial overgrowth technique was mounted inside the He-flow cryostat, and its temperature was kept at ~10 K for all measurements. Details on the linear optical properties of the sample have been reported in Ref. [30].

IV. EXPERIMENTAL RESULTS

A. Exciton OAM excited with single-mode LG pulses

We first consider the case for the single-mode LG pulse excitation: the pump pulse with $\ell_1 = -2$ and the probe pulse with $\ell_2 = +1$. The corresponding result has already been reported in Ref. [19]. In the report, we attributed origins of imperfect OAM conversions to $\ell = 0$ modes of the excitation pulses by comparing the results obtained using different excitation modes. Here, we focus on the decay dynamics of the exciton OAM, and as described below, we newly introduce the degree of OAM to evaluate the intrinsic exciton OAM dynamics.

Figure 2(a) illustrates the spectrum of the FWM signal and excitation pulse. The spectral peak of the excitation pulse is positioned between the heavy-hole exciton (X_{A}) resonance at 3.474 eV and light-hole exciton (X_{B}) resonance at 3.479 eV. The simultaneous excitations of X_{A} and X_{B} results in quantum beats (QBs) of FWM signals [23,24].

Figures 2(b) and 2(c) show the intensity profiles and OAM spectra of the pump and probe pulses, respectively. The distinct peaks in the OAM spectra indicate the successful single-mode generation of the $\ell_1 = -2$ pump and the $\ell_2 = +1$ probe pulses. In the experiment, second- and first-order-diffracted beams of a holographic grating with $\ell = +1$ were used to generate the $\ell_{1,2} \neq 0$ pump and probe pulse beams, respectively. We

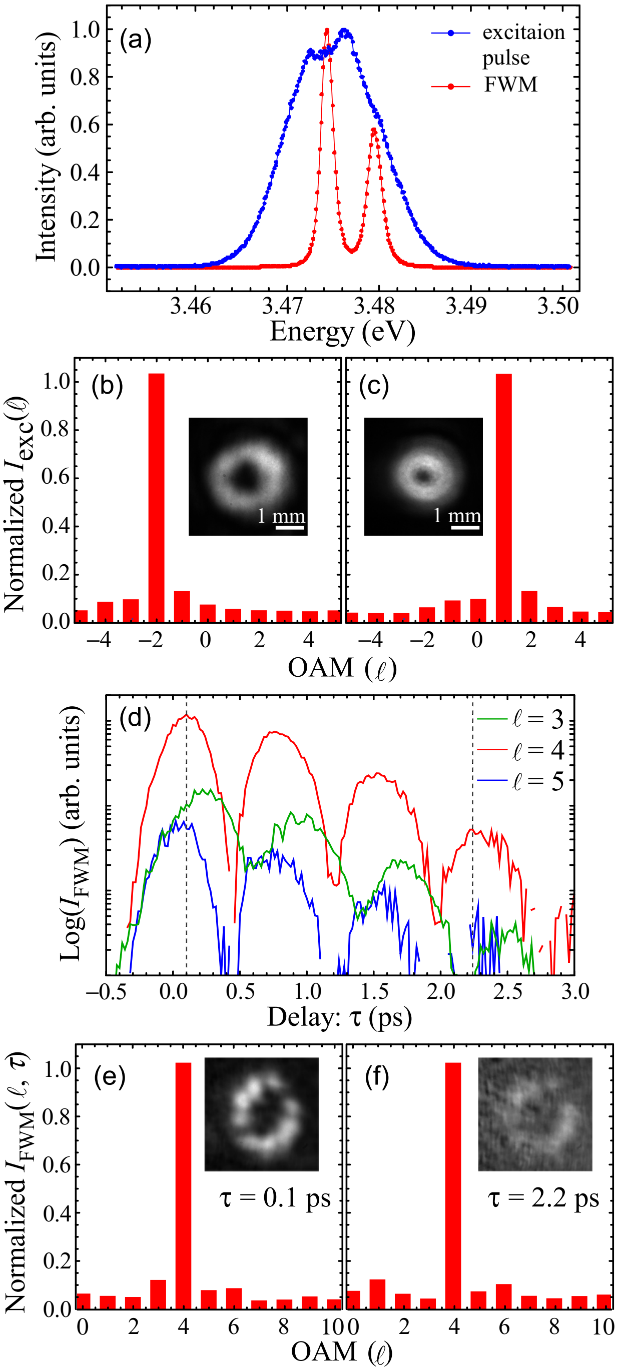

FIG. 2. (a) The spectrum of the four-wave mixing (FWM) signal. For reference, the spectrum of the excitation pulse is also overlaid. (b) The orbital angular momentum (OAM) spectrum of the pump pulse and (c) that of the probe pulse. For each spectrum, the vertical axis is normalized by its peak intensity. The insets show the intensity profiles of the corresponding beams. (d) The time evolutions of the OAM-resolved FWM signal (with a logarithmic vertical scale). In the figure, the $\ell = 3$, $\ell = 4$, and $\ell = 5$ components of the signal are plotted. (e),(f) The OAM spectra of the FWM signal at the selected delay time τ [the first and fourth QB peaks indicated by the dashed vertical lines in (c)]. The intensity profiles of the FWM signal are also shown in the insets.

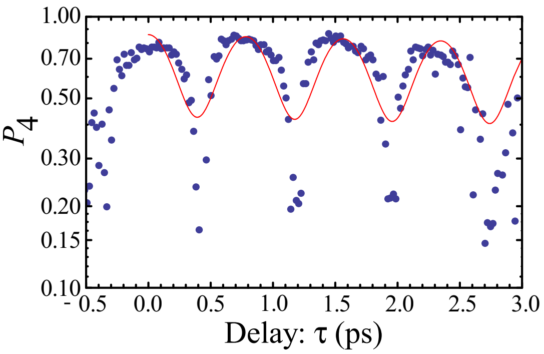

FIG. 3. The time evolution of the degree of the exciton orbital angular momentum (OAM) P_4 (with a logarithmic vertical scale). The solid curve indicates the sinusoidal exponential decay obtained by our fitting [31].

mention here that we added three extra mirrors in the optical path of the probe pulse to change the sign of ℓ_2 ($+2 \rightarrow -2$).

Figure 2(d) shows the time evolution of the OAM-resolved FWM signals for select values of ℓ, where the signal of X_{A} is displayed. A similar result is observed for X_{B}. In the figure, oscillations are observed for every value of ℓ, which are attributed to QBs. Upon fitting the sinusoidal exponential decay function, $[1+\cos(2\pi\tau/T_{\mathrm{QB}})]\exp(-2\tau/T_2)$, to the $\ell = \ell_{\mathrm{x}}(= 2\ell_2 - \ell_1) = +4$ component, we obtain the beating period $T_{\mathrm{QB}} = 0.75$ ps and the dephasing time $T_2 = 1.88$ ps, both of which are consistent with the spectral features.

It is important to note that in our previous work, we used the $\ell_i = 0$ mode as one of the excitation pulses and observed an intense $\ell = 0 \neq 2\ell_2 - \ell_1$ component in the OAM spectrum. This $\ell = 0$ anomaly is attributed to the contamination of the $\ell_i = 0$ mode in the excitation pulses [19]. In this experiment, we employed LG pulses with $\ell_i \neq 0$ for both the pump and probe pulses. As a result, we could strongly reduce the effect of $\ell = 0$ anomaly in the OAM spectra and thus more accurately evaluate the exciton OAM coherence.

Figures 2(e) and 2(f) show the OAM spectra of the FWM signal observed at the first and fourth QB peaks. The intensity profiles are also shown in the insets. The ring-shaped intensity pattern associated with the phase singularity is clearly observed, and the corresponding OAM spectrum indicates that the $\ell = \ell_{\mathrm{x}} = +4$ is distinct, thereby suggesting that the exciton OAM is nearly completely preserved at least up to $\tau = 2.5$ ps. This is also confirmed in Fig. 2(d), where the $\ell = +4$ component is predominant for most of the delay time τ. However, in these results, the decay dynamics of the OAM is unclear because the FWM signal is limited by T_2.

To extract the intrinsic OAM decay from the dephasing dynamics, we analyzed the degree of OAM, which is given by

$$P_n = \frac{W_n}{\sum_{q=-\infty}^{+\infty} W_q}, \tag{9}$$

where W_n denotes the spectral power weight of the $\ell = n$ component. The degree of OAM (P_n) is an excellent measure to evaluate the exciton OAM decoherence because P_n decreases with increasing OAM spectral broadening. Figure 3 shows the time evolution of P_4, wherein the summation is performed from $\ell = 0$ to 10 to preserve experimental accuracy. While the result clearly indicates that the OAM transfer is nearly perfect ($P_4 \approx 1$) within the dephasing time $T_2 \approx 1.9$ ps, it is also observed that P_4 slowly decreases with τ, thus indicating exciton OAM decoherence. When we assume that P_4 is governed by the exponential decay of $\exp(-2\tau/T_{\mathrm{OAM}})$, the OAM decay time T_{OAM} is evaluated to be 88 ± 3 ps. This value is considerably larger than the exciton dephasing time $T_2 \approx 1.9$ ps.

As pointed out in Sec. II, the coherence of the exciton OAM is lost due to the azimuthal variation in the dephasing $\gamma(r,\phi)$, meaning that the OAM decay reflects the global uniformity of the dephasing. Because we use the bulk GaN sample, the observed long OAM decay time, which is considerably longer than T_2, is reasonable. In fact, our previous strain-field analysis using a spatially resolved FWM suggests that the spatial variation in the exciton dephasing rate is small [32]. In other words, the decay of the exciton OAM allows us to evaluate the spatial uniformity of the sample with high sensitivity.

Further in Fig. 3, we also observe a periodic reduction in P_4, which is synchronized with the oscillation period of the QB. The periodic reduction in P_4 is thus attributed to the shifts of QB oscillation of the $\ell \neq \ell_{\mathrm{x}}(= +4)$ components. Indeed, the contaminant $\ell = +3$ component in Fig. 2(d) shows a small phase shift relative to $\ell = +4$. In general, the QB phase is sensitive to the spin-dependent exciton-exciton interactions [33]. For a typical example, in bulk GaN, the QBs in the colinear polarization excitation show no phase shift while the QBs in the cocircular polarization excitation show a shift between X_{A} and X_{B}. Since we use the colinear polarization configuration, the QBs ideally show no phase shift. However, the shift can arise if there is some spatial symmetry breaking (where the spin states are not well defined). Therefore, it is reasonable to consider that the contaminant component arises at the position with an azimuthal symmetry breaking, for example, around the localized potential, in which the effects of exciton correlation are expected to be enhanced [32]. Indeed we observed that the phase shift was changed depending on the location of the sample.

B. Exciton OAM excited with multiple-mode LG pump and single-mode Gaussian probe pulses

In the previous subsection, we observed the exciton OAM decoherence for $\ell_{\mathrm{x}} = 4$ and obtained the long OAM decay time T_{OAM}. Next, we demonstrate the ℓ_{x} dependence of the exciton OAM decoherence. The ℓ_{x} dependence of the exciton OAM decoherence is predicted from the uncertainty principle for the OAM and angular distribution, i.e., $\Delta\phi\Delta\ell \geqslant 1/2$ [34]. The details are discussed in the next section with the use of a simplified model for spatially dependent dephasing. In this subsection, we experimentally examine the ℓ_{x} dependence of the exciton OAM decoherence.

In order to compare the OAM decay for different values of ℓ_{x} under similar conditions concerning such as the spatial overlap between the pump and probe pulses, positions of the sample, and the sample temperature [21,22], we employed a multiple-mode LG pulse as the pump pulse. Furthermore, the multiple-mode pulse excitations allow simultaneous measurements for different values of ℓ_{x} while the sequential

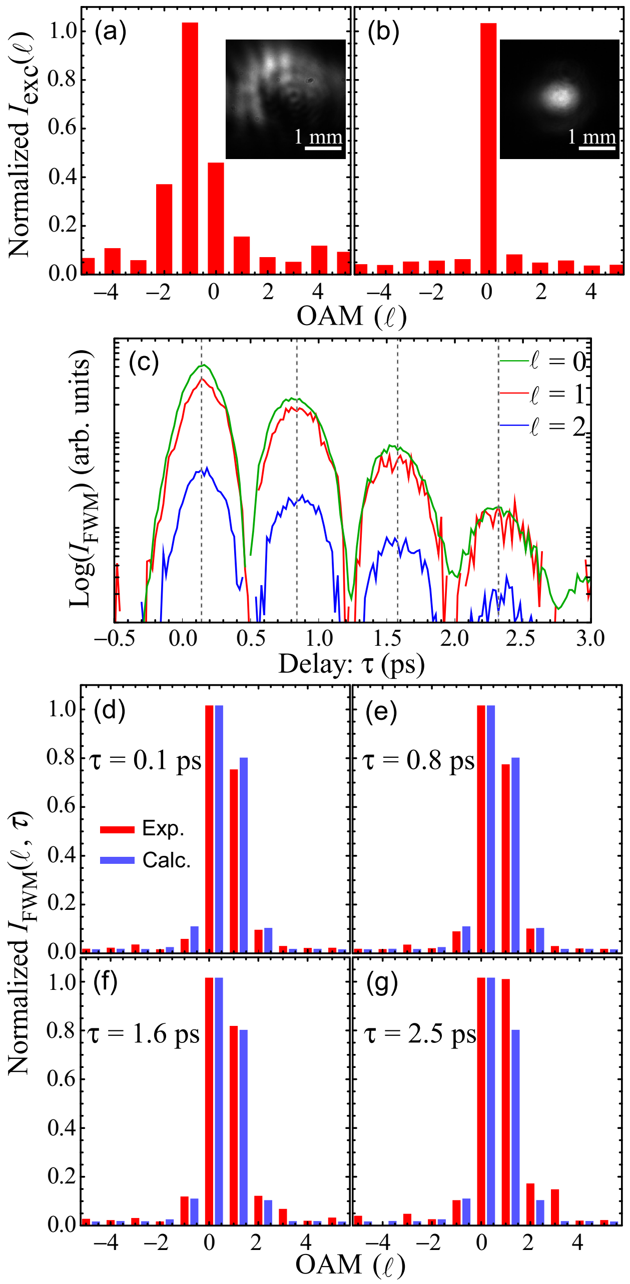

FIG. 4. (a) The orbital angular momentum (OAM) spectrum and intensity profile of the pump pulse. The angular extent of the pump pulse is restricted to π with an azimuthally restricted holographic grating. The spectral center is located at $\ell_1 = -1$ owing to the rotational phase modulation on the holographic grating. (b) The OAM spectrum and intensity profile of the probe pulse beam. (c) The time evolutions of the OAM-resolved FWM signal at $\ell = 0$, $\ell = 1$, and $\ell = 2$. (d)–(g) The OAM spectra of the FWM signal obtained for the different delay times τ indicated by the dashed vertical lines in (c). The numerically calculated OAM spectrum is also shown in each spectrum, where the differences of the decay time for different values of ℓ_x are not taken into account to emphasize the changes of the OAM spectra as a function of τ.

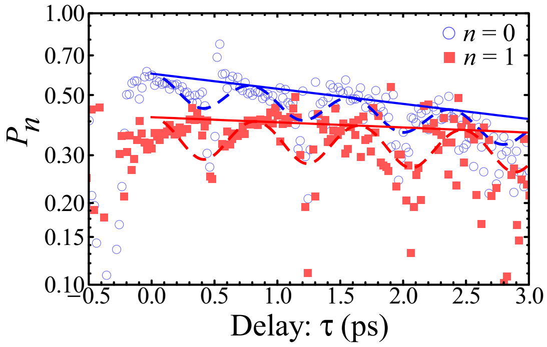

FIG. 5. The time evolutions of P_0 and P_1 (with a logarithmic vertical scale). The dashed curves indicate the sinusoidal exponential decays obtained by our fitting [36]. The solid lines are the exponential decays $\exp(-2\tau/T_{\mathrm{OAM}})$ extracted from the fitting curves and shown to highlight the difference of the decay times T_{OAM} between P_0 (15.6 ± 0.1 ps) and P_1 (46 ± 2 ps).

single-mode excitation with a distinct OAM cannot avoid the influences of, for example, long-term fluctuations of the laser. The OAM spectra of the pump and probe pulses are shown in Figs. 4(a) and 4(b), respectively. The OAM spectrum of the probe pulse exhibits a single peak at $\ell_2 = 0$ while that of the pump pulse shows the distribution resulting from the angular restriction of the beam [see the inset of Fig. 4(a)]. In order to obtain the OAM-resolved FWM signals with a similar intensity, we optimized the highest peak of the pump pulse to be located at $\ell_1 = -1$ by superimposing a fork dislocation on the angularly restricted grating [35]. In Fig. 4(a), the dominant components of the pump pulse are $\ell_1 = 0, \ -1$, and -2. Since the probe pulse beam can be approximately regarded as the pure $\ell_2 = 0$ mode, we expect that the FWM signal consists of $\ell_x = 2\ell_2 - \ell_1 = 0, \ +1$, and $+2$.

Figure 4(c) shows the time evolution of the OAM-resolved FWM signals at $\ell = 0, \ +1$, and $+2$. The result shows QB dynamics similar to that in Fig. 2(d). Figures 4(d)–4(g) show the OAM spectra obtained at the peak positions of the QB. One may consider that the OAM spectrum of the FWM signal is equal to that of the multiple-mode pump pulse with opposite sign ($\ell_x = 2\ell_2 - \ell_1 = -\ell_1$ when $\ell_2 = 0$). However, the FWM spectrum exhibits significant difference with respect to the pump spectrum, which arises from the topological charge dependence of the FWM conversion efficiency due to the difference of the spatial overlap between the LG modes given by $U_{\ell_1}(r)U_{\ell_2}^2(r)$ in Eq. (4). By using the OAM spectra of the excitation pulses in Fig. 4(a) and using Eq. (8), we calculate the OAM spectrum under the spatially uniform dephasing condition. As shown in Figs. 4(d)–4(g), the calculations well reproduce the experimental results. We note that the FWM signal intensities of the $\ell = 0$ and 1 components are nearly identical, and this allows us to compare the two components under similar excitation conditions [21,22].

Although the calculated spectrum well reproduces the experimental spectrum at $\tau = 0$, its time series shows some differences: For example, the $\ell = +1$ component at the fourth peak [Fig. 4(g)]. Moreover, the difference between the intensities for $\ell = 0$ and $\ell = +1$ decreases as the delay time increases, suggesting ℓ_x-dependent OAM decoherence. To clarify this hypothesis, we analyze the degrees of OAM in Fig. 5, where P_0 and P_1 are displayed as functions of τ. The time evolutions of P_0 and P_1 clearly show that the decay of the

$\ell_x = 0$ component is faster than that of the $\ell_x = 1$ component. Assuming the exponential decay function in the same manner as in the previous subsection, we evaluate the OAM decay time T_{OAM} to be 15.6 ± 0.1 ps and 46 ± 2 ps for P_0 and P_1, respectively. We note that while these decay times are exemplary and position dependent, the decay times for $\ell_x = 1$ are usually longer than those for $\ell_x = 0$.

V. ℓ_x-DEPENDENT EXCITON OAM DECAY

In Sec. IV B, we observed the ℓ_x dependence of the OAM decay time T_{OAM}. The OAM decay times for $\ell_x = 1$ are usually longer than those for $\ell_x = 0$. Although both the excitation condition and position of the sample are different from those in Sec. IV B, the degree of OAM P_4 in Sec. IV A exhibits the longest OAM decay time in our experiments. These results indicate that the exciton OAM decay time increases with increasing ℓ_x. In this section, using numerical calculations, we show that the spatially dependent dephasing results in such ℓ_x-dependent exciton OAM decoherence.

Figure 6 shows the ℓ_x dependence of the OAM decoherence in the presence of spatially dependent dephasing $\gamma(r,\phi)$. To easily understand this phenomenon, we employed a simplified model in which the spatial variation in γ was induced only by a pointlike defect located at (r_0,ϕ_0) and the exciton dephasing rate on the defect $\gamma(r_0,\phi_0)$ was different from that in the defect-free region [see the insets of Figs. 6(a)–6(c)]. As discussed in Sec. II, such spatially dependent dephasing modifies the angular distribution of exciton polarization and results in the OAM decoherence. We remark here that we only consider a single defect for $\gamma(r,\phi)$ although many defects may contribute to the signal. However, as shown in Sec. IV A, the profile of the FWM signal is nearly identical to that of an LG mode, thereby indicating that the number of defects that can modify the angular distribution of the exciton polarization [i.e., $P^{(3)}$ in Eq. (4)] is very limited. Therefore, we believe that our simplified model is reasonable for qualitative analysis. We note that the efficiency of the OAM decoherence (the OAM decay time) depends on the defect position (r_0,ϕ_0). In our model, the defect is located at the position where the most efficient OAM decoherence occurs for each value of ℓ_x.

We first consider the results of the numerical calculations for $\ell_x = 2\ell_2 - \ell_1 \neq 0$ in Figs. 6(e) and 6(f). When $\ell_x \neq 0$, $P^{(3)}$ in Eq. (4) corresponds to a ring-shaped distribution, and the defect located on the ring restricts the angular extent of the exciton center-of-mass motion at $\tau > 0$ [see Figs. 6(b) and 6(c)]. The resulting OAM spectra in Figs. 6(e) and 6(f) thus exhibit OAM spectral broadening, thereby indicating that the coherence of the exciton OAM with $\ell = \ell_x$ is partially lost. It is noteworthy that there is virtually no broadening if the defect is positioned near or far from the beam center since $P^{(3)}$ with $\ell_x \neq 0$ has no field amplitude. As for the ℓ_x dependence of the OAM decoherence, Figs. 6(e) and 6(f) indicate that the broadening reduces with increasing ℓ_x. The ℓ_x-dependent broadening can be understood by the uncertainty relationship $\Delta\phi\Delta\ell \geqslant 1/2$. Assuming that the pointlike defect has a finite size of a, $\Delta\phi$ is approximately $2\pi - a/\rho$, where ρ is given by Eq. (3). Since ρ is proportional to the square root of the topological charge ℓ_x, $\Delta\phi$ increases with increasing ℓ_x for the defect with fixed a. Consequently, the broadening decreases with increasing ℓ_x. In other words, the OAM coherence is robust against the spatially dependent dephasing $\gamma(r,\phi)$ for higher values of ℓ_x.

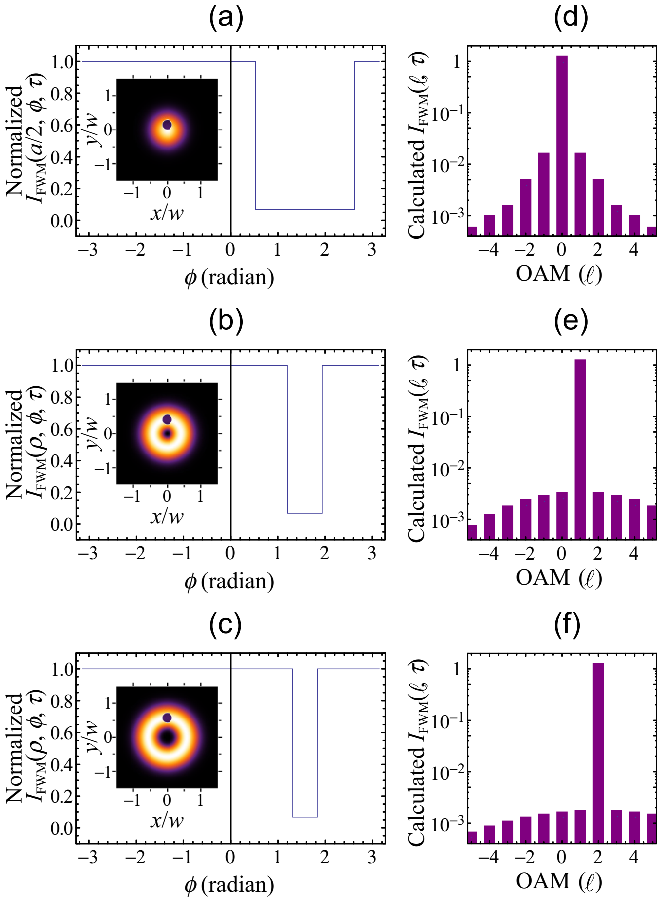

FIG. 6. (a)–(c) The calculated four-wave mixing (FWM) signals and their angular distributions at delay time $\tau > 0$ for $\ell_x = 0$, 1, and 2 including the effects of the spatially dependent dephasing. In the calculation, we use $\tau = 1/\gamma_0$ and the exciton dephasing rate in the defect $\gamma(r_0,\phi_0) = 2\gamma_0$, where γ_0 represents the exciton dephasing rate on the defect-free region. At $\tau > 0$, the signal intensity rapidly decays in the pointlike defect located at $(r,\phi) = (\rho,\pi/2)$ except for the case of $\ell_x = 0$. When $\ell_x = 0$, the defect is slightly shifted from the beam center by $a/2$. In the calculation, $\gamma_0 = 1$ and $a = 0.3w$ are used. (d)–(f) The OAM spectra calculated for the FWM signals shown in (a)–(c) with the use of Eq. (8). In the figures, we use a logarithmic vertical scale and the OAM-resolved intensity is normalized so that the maxima are equal to unity.

Next, we consider the case of $\ell_x = 0$. When $\ell_x = 0$, i.e., $P^{(3)}$ is described by a Gaussian field, the most efficient OAM decoherence occurs when the defect is positioned in the vicinity of the center of the field. We note that the defect at the exact field center shows no broadening due to its rotational symmetry. Since the pointlike defect is only slightly shifted from the center, the distribution of $P^{(3)}$ is restricted to a small angular extent, and thus, the broadening is large compared to the case of $\ell_x \neq 0$ [see Figs. 6(a) and 6(d)]. The above discussion suggests that the exciton OAM decay time T_{OAM} becomes larger with increasing ℓ_x. This prediction is consistent with our experimental results in Sec. IV.

VI. SUMMARY

In summary, we investigated the coherent dynamics of exciton OAM transferred by LG pulses via FWM in bulk GaN. To extract the intrinsic OAM decay from the dephasing dynamics, we analyzed the degree of the exciton OAM, which was derived from the OAM spectrum of the FWM signal. The result shows nearly a subnanosecond decay for $\ell = \ell_x = +4$, which is considerably longer than T_2. We also demonstrated the topological charge dependence of the exciton OAM dynamics, wherein a multiple-mode LG pulse was employed as the excitation pulse to compare the OAM decay for different values of ℓ_x. The decay of the $\ell = \ell_x = +1$ component is usually longer than that of the $\ell = \ell_x = 0$ component, thereby suggesting robustness of the exciton OAM. Both the observed long OAM decay time and its topological charge dependence are explained on the basis of the uncertainty relationship between the angular distribution and OAM. The angular extent of the exciton center-of-mass motion, which is determined by the azimuthal variation in the exciton dephasing, is large for larger ℓ_x. Consequently, the exciton OAM shows a smaller distribution, thereby resulting in a longer OAM decay time. This tendency was verified by the numerical calculations. On the other hand, the subnanosecond decay of the $\ell_x = +4$ exciton implies that the spatial variation in the dephasing is small in our bulk sample. In other words, the degree of the OAM allows us to evaluate the spatial uniformity of the dephasing even without scanning the sample. One straightforward way to test this ability is a comparison with a less spatially homogeneous sample, which will be investigated elsewhere.

ACKNOWLEDGMENT

This work was supported by a Grant-in-Aid for JSPS Fellows (Grant No. 14J11199) and CREST, JST.

---

[1] L. Allen, M. W. Beijersbergen, R. J. C. Spreeuw, and J. P. Woerdman, Phys. Rev. A **45**, 8185 (1992).
[2] G. F. Quinteiro and T. Kuhn, Phys. Rev. B **90**, 115401 (2014).
[3] L. Torner, J. P. Torres, and S. Carrasco, Opt. Express **13**, 873 (2005).
[4] K. Toyoda, F. Takahashi, S. Takizawa, Y. Tokizane, K. Miyamoto, R. Morita, and T. Omatsu, Phys. Rev. Lett. **110**, 143603 (2013).
[5] M. Watabe, G. Juman, K. Miyamoto, and T. Omatsu, Sci. Rep. **4**, 4281 (2014).
[6] T. Wang, L. Zhao, L. Jiang, and S. F. Yelin, Phys. Rev. A **77**, 043815 (2008).
[7] G. Gibson, J. Courtial, M. J. Padgett, M. Vasnetsov, V. Pas'ko, S. M. Barnett, and S. Franke-Arnold, Opt. Express **12**, 5448 (2004).
[8] J. Wang, J. Y. Yang, I. M. Fazal, N. Ahmed, Y. Yan, H. Huang, Y. Ren, Y. Yue, S. Dolinar, M. Tur, and A. E. Willner, Nat. Photon. **6**, 488 (2012).
[9] A. Mair, A. Vaziri, G. Weihs, and A. Zeilinger, Nature (London) **412**, 313 (2001).
[10] M. A. Noyan and J. M. Kikkawa, Appl. Phys. Lett. **107**, 032406 (2015).
[11] G. F. Quinteiro and J. Berakdar, Opt. Express **17**, 20465 (2009).
[12] M. B. Farías, G. F. Quinteiro, and P. I. Tamborenea, Eur. Phys. J. B **86**, 432 (2013).
[13] G. F. Quinteiro and P. I. Tamborenea, Europhys. Lett. **85**, 47001 (2009).
[14] G. F. Quinteiro, D. E. Reiter, and T. Kuhn, Phys. Rev. A **91**, 033808 (2015).
[15] N. B. Clayburn, J. L. McCarter, J. M. Dreiling, M. Poelker, D. M. Ryan, and T. J. Gay, Phys. Rev. B **87**, 035204 (2013).
[16] J. Wätzel, A. S. Moskalenko, and J. Berakdar, Opt. Express **20**, 27792 (2012).
[17] Y. Ueno, Y. Toda, S. Adachi, R. Morita, and T. Tawara, Opt. Express **17**, 20567 (2009).
[18] D. Persuy, M. Ziegler, O. Crégut, K. Kheng, M. Gallart, B. Hönerlage, and P. Gilliot, Phys. Rev. B **92**, 115312 (2015).
[19] K. Shigematsu, Y. Toda, K. Yamane, and R. Morita, Jpn. J. Appl. Phys. **52**, 08JL08 (2013).
[20] K. Leo, E. O. Göbel, T. C. Damen, J. Shah, S. Schmitt-Rink, W. Schäfer, J. F. Müller, K. Köhler, and P. Ganser, Phys. Rev. B **44**, 5726 (1991).
[21] S. T. Cundiff, H. Wang, and D. G. Steel, Phys. Rev. B **46**, 7248(R) (1992).
[22] Y. Z. Hu, R. Binder, S. W. Koch, S. T. Cundiff, H. Wang, and D. G. Steel, Phys. Rev. B **49**, 14382 (1994).
[23] A. J. Fischer, W. Shan, G. H. Park, J. J. Song, D. S. Kim, D. S. Yee, R. Horning, and B. Goldenberg, Phys. Rev. B **56**, 1077 (1997).
[24] K. Hazu, A. Shikanai, T. Sota, K. Suzuki, S. Adachi, S. F. Chichibu, and T. Mukai, Phys. Rev. B **65**, 195202 (2002).
[25] E. Yao, S. Franke-Arnold, J. Courtial, S. Barnett, and M. Padgett, Opt. Express **14**, 9071 (2006).
[26] G. Molina-Terriza, J. P. Torres, and L. Torner, Phys. Rev. Lett. **88**, 013601 (2001).
[27] G. C. G. Berkhout, M. P. J. Lavery, J. Courtial, M. W. Beijersbergen, and M. J. Padgett, Phys. Rev. Lett. **105**, 153601 (2010).
[28] K. Yamane, Z. Yang, Y. Toda, and R. Morita, New J. Phys. **16**, 053020 (2014).
[29] Y. Toda, K. Shigematsu, K. Yamane, and R. Morita, Opt. Commun. **308**, 147 (2013).
[30] K. Torii, T. Deguchi, T. Sota, K. Suzuki, S. Chichibu, and S. Nakamura, Phys. Rev. B **60**, 4723 (1999).
[31] For the fitting, we used the sinusoidal exponential decay given by $A[1 + B\cos(2\pi\tau/C)]\exp(-2\tau/T_{\mathrm{OAM}})$, where A, B, C, and T_{OAM} were the fitting parameters. Owing to the sinusoidal exponential decay, T_{OAM} can be evaluated not only in the dc but also in the ac frequencies, thereby increasing the accuracy of the T_{OAM} within the assumption that the OAM dynamics is governed by the exponential decay. When we fitted the Fourier-transformed P_4 to the Fourier-transformed fitting function, we obtained $A = 0.645$, $B = 0.333$, $C = 0.783$ ps, and $T_{\mathrm{OAM}} = 88$ ps.

[32] Y. Toda, K. Yamaguchi, T. Ishiguro, K. Hoshino, K. Tadatomo, and S. Adachi, Phys. Status Solidi C **6**, S684 (2009).

[33] T. Aoki, G. Mohs, M. Kuwata-Gonokami, and A. A. Yamaguchi, Phys. Rev. Lett. **82**, 3108 (1999).

[34] S. Franke-Arnold, S. M. Barnett, E. Yao, J. Leach, J. Courtial, and M. Padgett, New J. Phys. **6**, 103 (2004).

[35] B. Jack, M. J. Padgett, and S. Franke-Arnold, New J. Phys. **10**, 103013 (2008).

[36] The fitting curves for P_0 and P_1 were obtained in the same manner as P_4 in Sec. IV A. The fitting parameters for P_0 are $A = 0.535$, $B = 0.121$, $C = 0.795$ ps, and $T_{\mathrm{OAM}} = 15.6$ ps and those for P_1 are $A = 0.354$, $B = 0.169$, $C = 0.824$ ps, and $T_{\mathrm{OAM}} = 46$ ps.